Theoretical framework and jump relations for supersonic supercritical-fluid flows through shock waves

Kevin Foley-Valledor and Lluís Jofre*
Department of Fluid Mechanics, Universitat Politècnica de Catalunya · BarcelonaTech, Barcelona 08019, Spain

(Received 7 May 2026; accepted 14 October 2026; published 5 November 2026)

Shock waves have historically been modeled assuming ideal-gas behavior, yielding universal jump relations and a viscous structure that depends almost exclusively on the Mach number. However, many fluids of physical interest operate in dense or supercritical regimes where ideal-gas thermodynamics no longer applies. Therefore, this work investigates the structure of shock waves at supercritical-fluid conditions without invoking ideal-gas assumptions. Starting from the Navier-Stokes equations coupled with a real-fluid thermophysical model, the governing relations are derived for the spatial evolution of thermodynamic variables across the shock. Using supercritical carbon dioxide as a representative fluid, it is shown that nonideal thermodynamics strongly modifies the pressure-density jump relations and internal profiles of shocks, producing substantial deviations from classical Rankine-Hugoniot predictions. Interestingly, despite these pronounced thermodynamic effects, the physical thickness of the shock remains primarily controlled by the upstream Mach number. Taking both the structural and thermodynamic observations together, these results ultimately reveal how nonideal fluid behavior fundamentally alters compressive discontinuities, thereby establishing the strict limits of classical shock theory in dense and supercritical fluids.

DOI: 10.1103/cksm-mzc4

I. INTRODUCTION

Understanding the mechanisms governing flow acceleration, compression, and expansion in compressible regimes has enabled numerous technological developments. These include aerospace propulsion concepts such as hypersonic vehicle combustion systems [1], aerospike nozzles [2], and rotating detonation rocket engines [3]. Compressible flow phenomena are also central to several energy technologies, including inertial confinement fusion [4], detonation physics [5], and supercritical carbon dioxide power cycles [6]. Many of these systems operate in supersonic regimes where shock waves play a crucial role in dictating system performance. The fluid dynamics in these applications gain a profound level of complexity when the working fluid transitions into the supercritical regime. This state of matter, achieved at pressures P and temperatures T above the critical point (P_c and T_c), is a continuous phase region where intermolecular forces play a greater role, creating significant deviations from ideal-gas assumptions. In this regime, the locus of maximum isobaric heat capacity c_P, known as the pseudoboiling or Widom line [7], defines two

*Contact author: lluis.jofre@upc.edu

Published by the American Physical Society under the terms of the Creative Commons Attribution 4.0 International license. Further distribution of this work must maintain attribution to the author(s) and the published article's title, journal citation, and DOI.

different regions across which thermodynamic and transport properties vary significantly [8]: the liquidlike region and the gaslike region. The liquidlike region is characterized by large densities ρ, low isothermal compressibilities $\beta_T = (1/\rho)(\partial\rho/\partial P)_T$, and decreasing viscosity μ and thermal conductivity κ with increasing temperature [9]. In contrast, supercritical gaslike fluids exhibit lower densities and higher isothermal compressibilities, with transport coefficients that behave more similarly to those of a subcritical gas.

The Navier-Stokes equations provide a continuum description of fluid motion, where all their variables and their derivatives are continuous [10]. However, at high Reynolds numbers Re, regions characterized by steep gradients can develop with thicknesses δ that are infinitesimally small relative to the macroscopic length scale of motion L. In the inviscid limit $\mathrm{Re} \to \infty$, δ tends to zero, and these steep gradients manifest mathematically as flow discontinuities. In supersonic compressible flows, these discontinuities can appear in the form of shock waves, corresponding to thin compressive layers across which the flow velocity decreases abruptly while pressure, temperature, and density increase sharply. In the case of oblique shocks, these waves also induce flow deflection, a phenomenon extensively studied in classical aerodynamics [11]. The discontinuous changes in flow properties across these waves are strictly governed by the conservation laws of mass, momentum, and energy. Classical analytical descriptions treat the shock as an infinitesimally thin layer and typically assume ideal-gas behavior. While extremely weak shocks (characterized by low pressure and density ratios) generate negligible entropy and approximate isentropic compression, finite-strength shocks are fundamentally irreversible. Employing the Euler equations to conserve fluxes across the discontinuity yields the classical ideal-gas Rankine-Hugoniot jump relations [12,13]. These relations demonstrate that as shock strength increases, the pressure-density Hugoniot curve deviates significantly from an isentropic relation, asymptotically reaching a density ratio value of approximately 8. While this classical framework accurately predicts shock properties for low-density gases, it fails to capture the physics of dense and supercritical fluids, where highly nonlinear real-fluid thermodynamics fundamentally alters the jump relations and shock structure. The extension of classical shock theory to dense and supercritical fluids has motivated extensive work on real-fluid Riemann problems and nonideal compressible flows. Menikoff and Plohr [14] established that the thermodynamic properties of a general equation of state determine the isentropes and Hugoniot loci and consequently the admissible states connected by compressive waves. Subsequent developments have focused on the efficient numerical solution of real-fluid Riemann problems for compressible flow simulations, including neural-network approaches for calorically imperfect gases, supercritical fluids, and high explosives [15], as well as numerical formulations for compressible multiphase flows [16]. These studies primarily address the admissibility and propagation of macroscopic waves and therefore determine the equilibrium states connected by a shock rather than the internal finite-thickness structure between them.

Significant effort has been devoted to describing the internal structure of shock waves beyond the classical discontinuous approximation. Early theoretical developments established that viscosity and thermal conduction provide the mechanisms responsible for regularizing the shock transition [12,17,18]. This understanding led to the first continuous analytical solution of the one-dimensional Navier-Stokes equations by Becker [19], where transport properties were assumed constant. Later extensions incorporated temperature-dependent viscosity and thermal conductivity [20], establishing the classical description of shock waves as finite-thickness layers with characteristic scales of several molecular mean-free paths [21–23]. These formulations, however, were primarily developed within ideal-gas frameworks, limiting their applicability to dense and strongly nonideal fluids. To overcome these limitations, subsequent studies introduced additional thermodynamic and molecular effects into shock-wave modeling. Extensions including internal energy modes, such as vibrational and electronic excitation, demonstrated that molecular degrees of freedom can significantly modify the thermodynamic evolution and structure of high-speed shocks [24]. Similarly, continuum formulations incorporating nonideal equations of state have shown that real-fluid effects alter the velocity, temperature, and entropy profiles across the shock layer. For example, Anand and Yadav [25] derived analytical shock profiles using nonideal thermodynamic relations, while more

recent works by Khapra and Patel [26,27] incorporated dense-gas effects and internal molecular relaxation within Navier-Stokes-Fourier frameworks. These studies demonstrated that departures from ideal-gas behavior can modify the internal structure of shocks, although they generally focus on specific thermodynamic mechanisms or simplified equations of state with temperature-dependent transport coefficients. Related studies have further examined shock structure under specific nonideal thermodynamic or transport effects. Exact solutions for sonic shocks in van der Waals gases were obtained by Cramer and Sen [28], while Thompson *et al*. [29] investigated shock-induced phase changes in high-heat-capacity fluids using real-fluid equations of state. More recently, the roles of viscosity and heat conduction in determining the internal structure of shock waves have been examined systematically within the Navier-Stokes framework [30]. Real-fluid thermodynamics has also been incorporated into simulations of transcritical reacting and multiphase flows, where accurate equations of state and transport properties are required to describe high-pressure thermodynamics [31]. In these studies, however, the focus is generally placed on nonclassical wave behavior, molecular energy relaxation, multiphase effects, reacting flows, or the numerical solution of macroscopic flow problems, rather than on systematically resolving the finite-thickness structure of a normal shock across a range of dense-gas and supercritical thermodynamic states. Alternative approaches have considered kinetic descriptions of shock-wave structures, resolving the nonequilibrium behavior at molecular scales. While Navier-Stokes-based descriptions represent the accepted hydrodynamic limit [32,33], higher-order moment methods and kinetic formulations have been developed to capture nonequilibrium effects beyond continuum assumptions [34–36]. More recently, kinetic models have been extended towards dense and supercritical conditions, providing phase transition simulations in compressible flows [37]. These approaches provide valuable insight into molecular-scale mechanisms, but their complexity often limits their direct application to engineering-scale predictions of real-fluid shock structures. A major development in this area has been the emergence of nonideal compressible fluid dynamics, which specifically addresses flows involving dense gases and supercritical fluids near critical conditions [38]. In these regimes, strong molecular interactions modify the fundamental thermodynamic response of the fluid, affecting the convexity of the isentropic curves and the characteristics of wave propagation. As a consequence, nonclassical phenomena such as rarefaction shocks and modified shock admissibility conditions may arise [38,39]. Studies on the stability and dynamics of nonideal shocks have further shown that thermodynamic properties directly influence energy redistribution and acoustic behavior downstream of the shock [40,41]. Experimental investigations, such as those performed by Conti *et al*. [42], have confirmed that even moderate departures from ideal behavior can produce measurable modifications in shock intensity and total pressure losses. Despite these advances, most continuum-based analyses rely on simplified thermodynamic closures, including ideal-gas [22] or calorically-perfect-gas assumptions [43], with limited nonideal effects and often assuming fixed Prandtl numbers. Although real-fluid equations of state have been incorporated in some studies through models such as van der Waals–type formulations [44–46], these approaches often capture only limited aspects of real-fluid behavior. Consequently, a unified continuum framework that simultaneously describes the real-fluid jump relations and the viscous internal shock structure across subcritical, dense-gas, and supercritical regimes remains limited. Such a framework requires the consistent coupling of conservation laws with thermophysical properties evaluated from a complete real-fluid model, without relying on idealized assumptions. The present work addresses this specific aspect by considering the real-fluid normal-shock problem from the admissible upstream and downstream states to the continuous spatial transition connecting them. The Euler equations determine the real-fluid jump conditions for prescribed upstream pressure, temperature, and velocity, while the corresponding one-dimensional Navier-Stokes equations resolve the finite-thickness shock structure using local real-fluid thermodynamic and transport properties. This formulation makes it possible to analyze, within the same framework, how the upstream thermodynamic state modifies the magnitude of the shock and how the upstream flow velocity controls the spatial organization of the transition. In particular, the resulting analysis distinguishes the thermodynamic effects governing the jump amplitudes from the flow and transport-controlled effects governing shock

thickness and allows the thermodynamic trajectory through the supercritical region to be examined directly.

The objective of this work is therefore to characterize how dense-gas and supercritical thermodynamic conditions modify shock-wave behavior relative to classical ideal-gas predictions. The present formulation couples the one-dimensional Navier-Stokes equations with real-fluid thermophysical properties evaluated as functions of pressure and temperature, providing the basis for a systematic characterization of finite-thickness shock waves across different thermodynamic states. This enables the simultaneous characterization of the macroscopic jump relations and the internal shock structure across a wide range of upstream conditions from subcritical to supercritical regimes, including liquidlike and gaslike conditions. By resolving the shock structure for different combinations of upstream pressure, temperature, and velocity, this framework allows the individual influence of thermodynamic state and flow intensity to be assessed. Carbon dioxide is selected as a representative fluid due to its well-characterized supercritical behavior and accessible critical conditions, with a critical pressure of $P_c = 7.4$ MPa and a critical temperature of $T_c = 304.1$ K. The resulting analysis provides insight into how deviations from ideal-gas behavior affect shock intensity, thermodynamic profiles, and thickness, establishing a consistent continuum description of shock-wave structures in dense and supercritical fluids.

The remainder of the paper is organized as follows. Section II presents the mathematical framework, including the fundamental equations of fluid motion and the mean-free-path equation that serves as the characteristic length scale of the phenomenon. Section III introduces the shock-centered formulation and derives the equations governing the internal structure. Section IV analyzes the jump relations in real fluids and their deviation from classical models, providing the boundary conditions to the real-fluid shock structure problem. Section V resolves the equations developed in Sec. III, with the boundary conditions from Sec. IV, and examines the evolution of thermophysical properties and shock thickness across different regimes. Section VI summarizes our work, discusses our findings, and offers prospects for future work.

II. FLOW PHYSICS MODELING

The framework utilized for studying supersonic supercritical-fluid flows through shock waves in terms of (i) the equations of fluid motion and (ii) the mean-free path is detailed below.

A. Equations of fluid motion

Characterizing the internal structure of shock waves requires a modeling framework based on the fundamental equations of fluid motion, which can be expressed in terms of the nondimensional equations for the conservation of mass, momentum, and total energy as

$$\frac{\partial \rho^\star}{\partial t^\star} + \nabla^\star \cdot (\rho^\star \boldsymbol{u}^\star) = 0, \tag{1a}$$

$$\frac{\partial (\rho^\star \boldsymbol{u}^\star)}{\partial t^\star} + \nabla^\star \cdot (\rho^\star \boldsymbol{u}^\star \boldsymbol{u}^\star) = -\nabla^\star P^\star + \frac{\nabla^\star \cdot \boldsymbol{\tau}^\star}{\mathrm{Re}}, \tag{1b}$$

$$\frac{\partial (\rho^\star E^\star)}{\partial t^\star} + \nabla^\star \cdot (\rho^\star \boldsymbol{u}^\star E^\star) = -\frac{\nabla^\star \cdot \boldsymbol{q}^\star}{\mathrm{Re\,Br}} - \nabla^\star \cdot (P^\star \boldsymbol{u}^\star) + \frac{\nabla^\star \cdot (\boldsymbol{\tau}^\star \cdot \boldsymbol{u}^\star)}{\mathrm{Re}}, \tag{1c}$$

where the star superscript denotes quantities normalized by their respective reference values. The primary flow variables are the density ρ, time t, velocity vector $\boldsymbol{u}$, pressure P, and total energy E. The viscous stress tensor is defined as $\boldsymbol{\tau} = \mu(\nabla \boldsymbol{u} + \nabla^T \boldsymbol{u}) + \mu'(\nabla \cdot \boldsymbol{u})\boldsymbol{I}$, where $\mu' = \mu_v - \frac{2}{3}\mu$ is the second coefficient of viscosity expressed in terms of the bulk viscosity μ_v and the dynamic viscosity μ. Furthermore, $\boldsymbol{q} = -\kappa \nabla T$ represents the Fourier heat-conduction flux for a single-species fluid, with κ the thermal conductivity and T the temperature. This nondimensionalization introduces specific dimensionless numbers, such as the Reynolds number $\mathrm{Re} = \rho_{\mathrm{ref}} u_{\mathrm{ref}} l_{\mathrm{ref}} / \mu_{\mathrm{ref}}$, which relates the inertial to viscous forces, and the Brinkman number $\mathrm{Br} = \mu_{\mathrm{ref}} u_{\mathrm{ref}}^2 / \kappa_{\mathrm{ref}} T_{\mathrm{ref}}$, representing the ratio

of viscous dissipation to molecular heat conduction. Here the subscript ref denotes the reference values of the properties. In this work, body forces such as gravity or Coriolis effects do not play a significant role and are thus neglected.

This set of fluid motion equations requires a thermodynamic closure model. In this regard, pressure, temperature, and density are related through a real-fluid equation of state. After nondimensionalization, a generalized real-fluid equation of state can be written as [47]

$$P^\star = \frac{Z\rho^\star T^\star}{\hat{\gamma}\,\mathrm{Ma}^2}, \tag{2}$$

where $\hat{\gamma} \approx Z(c_P/c_V)[Z + T(\partial Z/\partial T)_\rho/Z + T(\partial Z/\partial T)_P]$ is an approximated real-fluid heat capacity ratio [48], with c_P and c_V the specific isobaric and isochoric heat capacities, respectively. The Mach number, characterizing the ratio of the flow velocity to the speed of sound c, is given by $\mathrm{Ma} = u_{\mathrm{ref}}/c_{\mathrm{ref}}$. Finally, Z is the compressibility factor, which can be evaluated using real-fluid equations of state, such as the Soave-Redlich-Kwong [49] and Peng-Robinson [50] equations of state, or reference libraries like CoolProp [51] and NIST [52].

B. Mean-free path

The spatial scales associated with shock waves can approach molecular dimensions. Consequently, the thickness of these discontinuities is expected to be on the order of several molecular mean-free paths [22,43]. For a single-species fluid, the molecular mean-free path can be approximated as [8]

$$\lambda \approx \frac{k_B T Z}{\sqrt{2}\pi d^2 P}, \tag{3}$$

where $k_B = 1.380\,649 \times 10^{-23}$ J/K is the Boltzmann constant and $d = 0.33$ nm the particle hard-shell diameter for the CO_2 molecule [9]. This equation is expressed in terms of the primitive thermodynamic variables P, T, and Z, rather than its equivalent formulation in terms of density, which would reduce the expression to a dependence proportional to $1/\rho$. This representation is adopted to remain consistent with the real-fluid thermodynamic framework, where all properties are evaluated as functions of pressure and temperature. Furthermore, using P and T as the independent thermodynamic variables facilitates the mapping of the fluid state within phase diagrams and the evaluation of thermophysical properties from real-fluid databases.

Equation (3) indicates that the molecular mean-free path depends on both pressure and temperature. To quantify this dependence, utilizing Z values from NIST [52], the mean-free path is plotted as a function of reduced temperature for various reduced pressures in Fig. 1, alongside the ideal-gas case ($Z = 1$) for comparison. At subcritical temperatures, the real-fluid curves collapse, yielding similar mean-free-path values. However, in the vicinity of the critical point, abrupt variations are observed, corresponding to second-order transitions across the pseudoboiling line between the supercritical liquidlike and gaslike phases. Under high-pressure conditions, molecular proximity leads to smoother property transitions and a slower rate of increase for the mean-free path. These results highlight the importance of accounting for variations in the mean-free path when studying a wide range of thermodynamic states. Nevertheless, the specific cases examined in this work fall within a regime where the mean-free path does not vary drastically. While the typical thickness of a shock wave is on the order of several mean-free paths, the expected variations in the mean-free path across the considered conditions are approximately on the order of 0.1–1 nm. To maintain a clear focus on core physical trends, this study prioritizes a qualitative analysis over an exhaustive quantitative comparison of exact dimensional thicknesses. Nonetheless, the interested reader can retrieve exact physical dimensions by rescaling the nondimensionalized thickness with the local mean-free path. Finally, it is worth noting the discrepancy between the real-fluid and ideal-gas mean-free-path predictions; this difference is most pronounced at low pressures, and the two models only yield comparable values at high temperatures within the supercritical gaslike region.

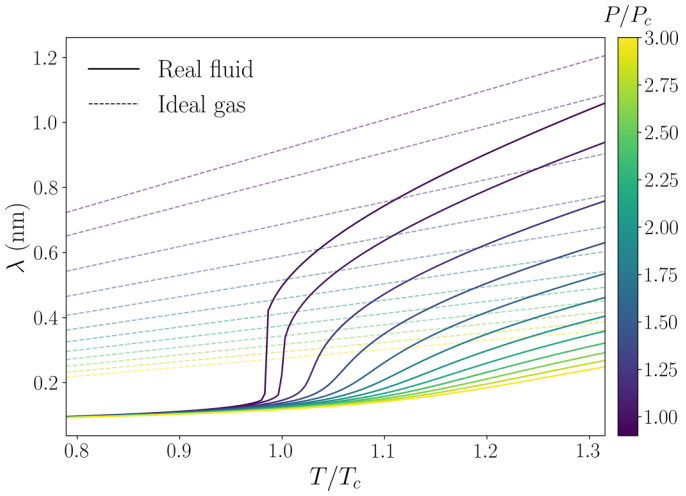


FIG. 1. Variation of the mean-free path λ for CO_2 as a function of reduced temperature T/T_c, for different reduced pressures P/P_c. Solid lines represent real-fluid behavior, while dashed lines correspond to ideal-gas ($Z = 1$) calculations.

III. REAL-FLUID SHOCK-WAVE FORMULATION

This section details the methodological approach adopted to investigate supersonic supercritical-fluid flows across shock waves, focusing on (i) the underlying hypotheses and (ii) the conservation equations for the shock-wave structures.

A. Hypotheses

The mathematical analysis of shock waves in supercritical fluids is simplified by adopting a shock-centered reference frame. The structure and impact of such complex discontinuity phenomena depend directly on the upstream conditions which, when fixed, yield a unique normal shock solution. By assuming uniform steady-state conditions far upstream, the transient terms vanish, making all spatial derivatives null and resulting in a zero-velocity divergence, i.e., $\boldsymbol{\nabla}^\star \cdot \boldsymbol{u}^\star = 0$. Consequently, the bulk viscosity becomes negligible in the upstream region and only becomes physically relevant within the shock-wave layer itself, where steep velocity variations occur. Despite this localized relevance, there is currently limited consensus on bulk viscosity models near the critical point, especially for CO_2 [53,54]. Nevertheless, the theoretical framework developed in this work is formulated generally, allowing for the incorporation of any specific bulk viscosity model. As more accurate thermodynamic data and models become available, they can be readily integrated into these equations to further refine the resolution of shock-wave structures. Finally, the flow is assumed to be one dimensional, enabling the study of the internal shock structure through the one-dimensional (1D) conservation equations.

B. Conservation equations for shock-wave structures

To resolve the internal structure of the shock wave, the corresponding upstream and downstream boundary conditions must first be established. By definition, a shock wave is a compressive discontinuity across which fluid properties change abruptly. To determine these jump relations, uniform upstream and downstream conditions are assumed, resulting in the following set of nondimensional

1D steady-state Euler equations:

$$\rho^\star_{\rm us} u^\star_{\rm us} = \rho^\star_{\rm ds} u^\star_{\rm ds}, \tag{4a}$$

$$P^\star_{\rm us} + \rho^\star_{\rm us} {u^\star_{\rm us}}^2 = P^\star_{\rm ds} + \rho^\star_{\rm ds} {u^\star_{\rm ds}}^2, \tag{4b}$$

$$h^\star_{\rm us} + \tfrac{1}{2} {u^\star_{\rm us}}^2 = h^\star_{\rm ds} + \tfrac{1}{2} {u^\star_{\rm ds}}^2. \tag{4c}$$

These expressions are derived from the inviscid limit of the fluid motion equations (1) under steady and uniform assumptions. They describe the macroscopic flow states at the boundaries of the system, specifically far upstream and downstream.

Once the upstream and downstream boundary conditions are defined, the internal structure of the shock wave can be resolved. From the 1D steady-state conservation equations (1), the mass-conservation equation (1a) yields a constant mass flux ρu. Furthermore, assuming no external heat addition, the enthalpy formulation of Eq. (1c) demonstrates that the stagnation enthalpy is conserved across the domain, rendering the shock adiabatic. Integrating this energy equation alongside the momentum equation (1b), normalizing with respect to upstream values, and applying algebraic manipulation yields the nondimensional equation for the spatial evolution of temperature in a shock-centered reference frame as

$$\frac{dT^\star}{d\xi^\star} = \frac{{\rm Re}_{\lambda,{\rm us}} {\rm Br}_{\rm us}}{\kappa^\star} \left((h^\star - h^\star_{\rm us}) - \frac{(u^\star - 1)^2}{2} - u^\star (P^\star - P^\star_{\rm us}) \right), \tag{5}$$

where $\xi^\star = x/\lambda_{\rm us}$ is the nondimensional spatial coordinate, ${\rm Re}_{\lambda,{\rm us}} = \rho_{\rm us} u_{\rm us} \lambda_{\rm us} / \mu_{\rm tot,us}$ is the upstream molecular Reynolds number with $\mu_{\rm tot} = \mu_v + \frac{4}{3}\mu$ the total viscosity, and ${\rm Br}_{\rm us} = \mu_{\rm tot,us} u^2_{\rm us} / \kappa_{\rm us} T_{\rm us}$ is the upstream local Brinkman number.

Combining Eq. (5) with the integrated enthalpy equation yields the nondimensional spatial distribution of velocity in the form

$$\frac{du^\star}{d\xi^\star} = \frac{{\rm Re}_{\lambda,{\rm us}}}{\mu^\star_{\rm tot}} [(1 - u^\star) + (P^\star - P^\star_{\rm us})]. \tag{6}$$

Under the calorifically-perfect-gas assumption, Eq. (6) reduces to the classical formulations derived in previous studies [22,43].

The final nondimensional equation required to close the system describes the spatial variation of pressure. It is derived from Eq. (1a) and is expressed as

$$\frac{dP^\star}{d\xi^\star} = \frac{1}{\rho^\star \beta^\star_T} \frac{d\rho^\star}{d\xi^\star} + \frac{\alpha^\star_T}{\beta^\star_T} \frac{dT^\star}{d\xi^\star}, \tag{7}$$

where $\beta^\star_T = \frac{1}{\rho^\star} \frac{\partial \rho^\star}{\partial P^\star}|_{T^\star}$ is the isothermal compressibility and $\alpha^\star_T = -\frac{1}{\rho^\star} \frac{\partial \rho^\star}{\partial T^\star}|_{P^\star}$ is the thermal expansion coefficient. A detailed derivation of this formulation is provided in Appendixes A and B for real and ideal fluids, respectively. The resulting system of three equations involves four flow variables $T^\star$, $h^\star$, $u^\star$, and $P^\star$. To close the system of equations, the dimensionless enthalpy is expressed as a function of the local dimensionless pressure and temperature, $h^\star = (P^\star, T^\star)$. Because real-fluid analysis precludes the use of ideal-gas approximations, this system must be solved numerically. To achieve this, the thermodynamic properties are evaluated using experimental data extracted from the NIST database [52]. Finally, an open-source solver developed specifically to resolve these equations is available for the interested reader from Ref. [55].

IV. RANKINE-HUGONIOT RELATIONS IN REAL FLUIDS

Carbon dioxide is selected as a representative fluid due to its well-characterized thermodynamic behavior and accessible critical conditions, which make it an ideal candidate to explore strong real-fluid effects. It should be noted that this fluid does not exhibit the strong nonconvex thermodynamic regions associated with Bethe-Zel'dovich-Thompson fluids [56], for which the

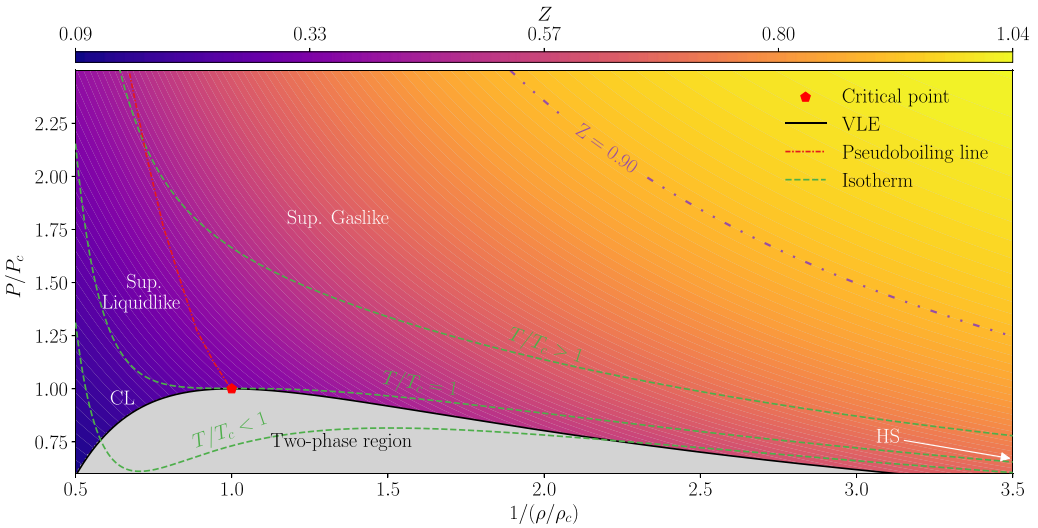


FIG. 2. Phase diagram of CO_2 representing supercritical, critical, and subcritical isotherms. Compressed liquid (CL), superheated steam (HS), supercritical liquidlike, supercritical gaslike, and two-phase regions are indicated. The colormap portrays the distribution of the compressibility factor Z. All variables are normalized with their critical values.

fundamental derivative of gas dynamics may become negative and nonclassical wave phenomena such as rarefaction shocks can occur [38]. Nonetheless, the insight and results obtained with CO_2 can be generalized to a wide range of substances through the principle of corresponding states [57], viz., most fluids, when compared at the same $T_r = T/T_c$ and $P_r = P/P_c$, (i) have approximately the same compressibility factor Z and (ii) all deviate similarly from ideal gas. Figure 2 presents its phase diagram, where different thermodynamic regions are identified together with a colormap of the compressibility factor Z. The strong spatial variation of Z across the diagram highlights substantial departures from ideal-gas behavior and anticipates significant modifications of the flow physics depending on the upstream thermodynamic state.

This thermodynamic complexity directly impacts the structure of shock-wave jump relations. In classical formulations based on ideal-gas assumptions, both isentropic and Rankine-Hugoniot relations depend on a single upstream thermodynamic variable, as the equation of state reduces to a simple pressure-density relation. In contrast, for real fluids, the solution depends on both pressure and temperature, through $h = h(P, T)$ in Eq. (4c), and the jump conditions therefore become functions of the full thermodynamic state. As a result, the downstream solution and the associated shock structure cannot be determined without a complete specification of the upstream conditions, effectively introducing an additional thermodynamic degree of freedom into the problem. To account for real-fluid effects, all thermodynamic and transport properties, including the speed of sound, are evaluated as functions of pressure and temperature, i.e., $\mathrm{f} = \mathrm{f}(P, T)$, using data extracted from the NIST database [52]. The Mach number is therefore defined using the local real-fluid speed of sound, which varies throughout the shock structure.

The implications of this behavior can be analyzed through the Euler equations, which define the admissible jump conditions at the shock boundaries [Eq. (4)]. These are general relations applicable to a real fluid at the boundaries and provide the solution to the jump relations, which greatly differ from the Rankine-Hugoniot or isentropic relations under conditions far from ideal gas. In the present formulation, these relations are used to establish the boundary conditions for the finite-thickness shock structure resolved subsequently in Sec. V. The behavior of the jump relations is illustrated in Fig. 3, where the pressure jump ratio is represented as a function of the density ratio

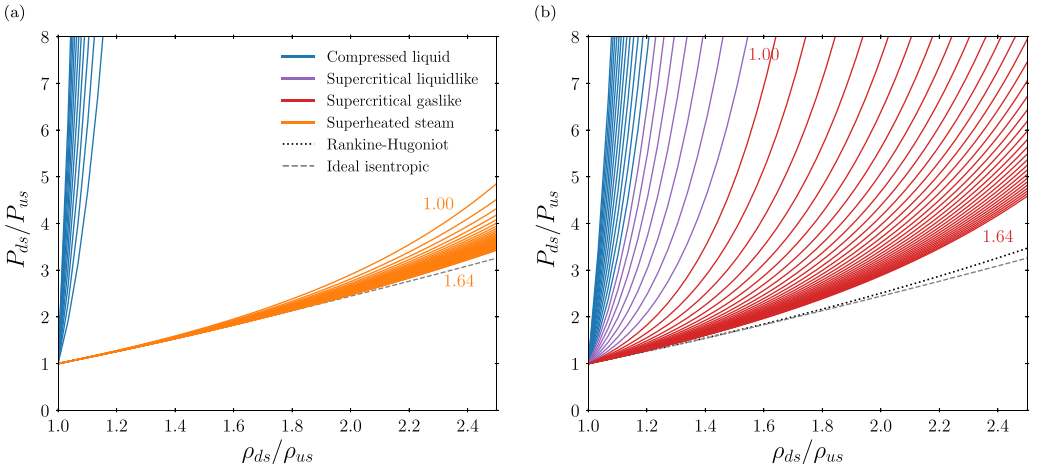


FIG. 3. Jump relation distribution, regarding Euler's energy-conservation equation (4c), for different upstream reduced temperatures, at (a) $P_{\mathrm{us}}/P_c = 0.8$, portraying two differentiated phases, i.e., compressed liquid in blue and superheated steam in orange, and (b) $P_{\mathrm{us}}/P_c = 2$, portraying compressed liquid in blue, supercritical liquidlike in purple, and supercritical gaslike in red. Both sets of curves are compared to ideal isentropic and Rankine-Hugoniot relations.

for different reduced upstream temperatures. Under subcritical conditions [Fig. 3(a)], two distinct regimes emerge. In the compressed liquid region, the fluid exhibits low compressibility due to strong intermolecular interactions, resulting in large pressure increases for relatively small density variations across the shock. Conversely, in the superheated steam region, increasing temperature rapidly drives the fluid towards ideal-gas behavior, reducing intermolecular effects and recovering classical-like jump ratios. This transition is consistent with the trends observed in Fig. 2, where the compressibility factor approaches unity as temperature increases. Nevertheless, the tendency of the Z isolines indicates that, as the upstream pressure decreases, the temperature needed to achieve ideal behavior is lower.

The behavior becomes more intricate in the supercritical regime [Fig. 3(b)], where no phase boundary exists but distinct liquidlike and gaslike regions can still be identified. In this case, only supercritical gaslike states approach the ideal limit, as they approximate the $Z = 1$ isoline in Fig. 2. In contrast, the supercritical liquidlike region remains strongly nonideal and significantly deviates from the isentropic or Rankine-Hugoniot curves. This demonstrates that even in the absence of phase interfaces, the thermodynamic landscape continues to play a dominant role in determining the shock behavior. Overall, these results show that the classical picture of shock-wave jump relations as functions of a single parameter breaks down in real fluids. Instead, the shock intensity and admissible states are governed by the specific thermodynamic state that defines the upstream region.

Once the thermodynamic state of the fluid is fully characterized, the admissible downstream conditions are determined by the conservation constraints imposed across the shock. In particular, combining Eq. (6) with the assumption of uniform flow at the boundaries yields a relation between pressure and density jumps as a function of the upstream Mach number expressed as

$$\frac{P_{\mathrm{ds}}}{P_{\mathrm{us}}} \approx \left(1 - \frac{\rho_{\mathrm{us}}}{\rho_{\mathrm{ds}}}\right) \frac{\hat{\gamma}_{\mathrm{us}} \mathrm{Ma}_{\mathrm{us}}}{Z_{\mathrm{us}}} + 1, \tag{8}$$

which can also be derived from Eq. (4b). In contrast with ideal-gas studies [17], this expression explicitly incorporates real-fluid physics through the compressibility factor Z_{us} and the effective heat capacity ratio $\hat{\gamma}_{\mathrm{us}}$. Physically, this reflects the influence of intermolecular interactions and nonlinear thermodynamic behavior on momentum transfer across the shock. In particular, deviations

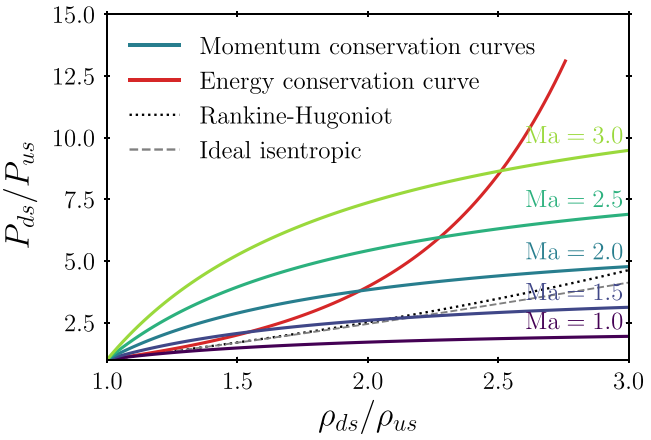


FIG. 4. Combination of Euler's energy- and momentum-conservation equations (4b) and (4c) at upstream conditions $P_{\text{us}}/P_c = 2$ and $T_{\text{us}}/T_c = 1.3$. The intersection of the curves provides the real-fluid jump ratios.

of Z from unity alter the effective compressibility of the fluid, thereby modifying the pressure response required to accommodate a given density change. Similarly to Euler's energy-conservation relation (4c), the momentum-conservation curves indicate the admissible solutions. This solution is finally the result of the unique intersection between the energy- and momentum-conservation curves under given upstream pressure, temperature, and velocity conditions. As a result, the jump relations are characterized for every upstream state in a real fluid. This behavior is illustrated in Fig. 4, where different momentum curves, parametrized by Ma_{us}, intersect a given energy curve defined by $(P_{\text{us}}, T_{\text{us}})$. As Ma_{us} increases, these intersections shift towards higher pressure ratios, leading to stronger shocks. However, the deviation from ideal-gas predictions is not driven by the Mach number itself but by the thermodynamic relation encoded in the energy equation. At the same time, the momentum constraint is altered through the compressibility factor Z_{us}, which directly affects the pressure response for a given density change. Equation (8) shows that reductions in Z_{us} amplify the required pressure increase, reflecting the reduced compressibility of the fluid. As a result, while increasing Mach number intensifies the shock, real-fluid thermodynamics determines how much stronger the shock is compared to the ideal-gas prediction.

V. THERMOFLUID CHARACTERIZATION OF SHOCK WAVES

The thermofluid characterization of shock-wave structures is determined by (i) the evolution of thermophysical properties across the shock and (ii) the thickness of the structure.

A. Evolution of thermophysical properties

The determination of the jump conditions in real fluids establishes the upstream and downstream states that bound the shock and therefore provides the necessary closure to resolve its internal structure through Eqs. (5)–(7). Once these boundary states are fixed, the problem reduces to describing how the flow variables transition between them within the shock layer. Within this framework, the variables naturally follow a hyperbolic tangent shape with the shock centered and the profiles evolving between two asymptotic states. As a result, all variables exhibit monotonic profiles with steep gradients concentrated within a narrow region around the shock. This behavior reflects the balance between convective transport, which steepens gradients, and diffusive mechanisms, which regularize the discontinuity over a finite thickness. The structure and intensity of the shock can therefore be directly related to the upstream conditions through Eqs. (5) and (6). In particular, increasing the upstream velocity u_{us} leads to a linear growth of the molecular Reynolds number

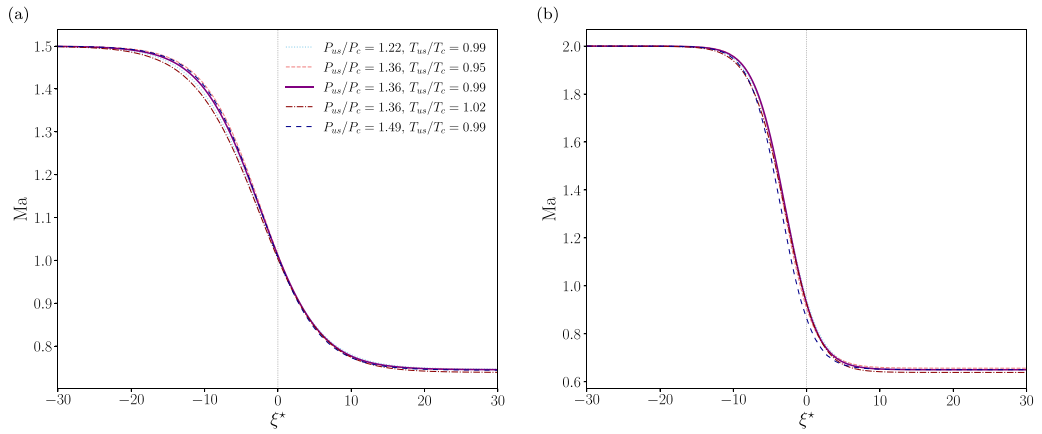


FIG. 5. Velocity profiles in terms of Mach number for different upstream conditions, computed for (a) $\mathrm{Ma}_{\mathrm{us}} = 1.5$ and (b) $\mathrm{Ma}_{\mathrm{us}} = 2.0$.

$\mathrm{Re}_{\lambda,\mathrm{us}}$ and a quadratic increase of the Brinkman number $\mathrm{Br}_{\mathrm{us}}$. This scaling indicates that inertial transport and viscous dissipation become progressively more dominant relative to diffusive processes, thereby reducing the ability of viscosity and thermal conduction to smooth spatial gradients. As a consequence, steeper gradients develop and the shock thickness decreases with increasing upstream velocity. Independently, as the flow decelerates across the shock, the pressure and enthalpy terms compensate for the drastic loss of kinetic energy, rapidly increasing pressure and temperature. This energy redistribution governs the amplitude of the thermodynamic changes, while the spatial structure remains controlled by the transport balance.

These effects are illustrated in Fig. 5, which shows the velocity profiles with respect to the sound speed for different upstream Mach numbers and thermodynamic states. As can be observed, for increasing $\mathrm{Ma}_{\mathrm{us}}$, the profiles become progressively steeper, confirming the reduction in shock thickness. In contrast, variations in the upstream thermodynamic state have a negligible impact on the velocity profiles, indicating that the shock structure is primarily controlled by the flow velocity, with thermodynamic effects playing a secondary role in shaping the profiles. While the physical width of the shock is primarily controlled by the upstream Mach number, the upstream thermodynamic state introduces secondary modifications to the magnitude of the property variations across the discontinuity. The distinction is evident in Fig. 6, where variations in upstream pressure and temperature modify the amplitude of the profiles without significantly altering their spatial extent: Fig. 6(a) represents the pressure jump, while Fig. 6(b) represents the temperature jump. In particular, an increase in upstream pressure P_{us} amplifies the pressure jump across the shock, leading to more intense compressions. In contrast, an increase in the upstream temperature T_{us} has a mitigating effect on the strength of the shock, as reflected in lower pressure and temperature ratios. These trends are consistent with the jump relations discussed in Fig. 3, where higher pressures lead to more pronounced energy curves, resulting in stronger shocks. In contrast, increasing temperature drives the fluid towards more ideal behavior, reducing the deviation from Rankine-Hugoniot predictions and consequently weakening the shock. However, these thermodynamic effects act as secondary corrections to the dominant role of the upstream velocity. As shown in Fig. 5, variations in $\mathrm{Ma}_{\mathrm{us}}$ produce significantly larger changes in both the shock thickness and the magnitude of the profiles than those induced by thermodynamic variations. Therefore, while pressure and temperature determine the direction and magnitude of deviations from ideal behavior, the upstream velocity remains the primary parameter controlling both the structure and the overall intensity of the shock.

Finally, the density evolution provides additional insight into the thermodynamic path followed across the shock. As shown in Fig. 7(a), the density profiles exhibit relatively small variations across

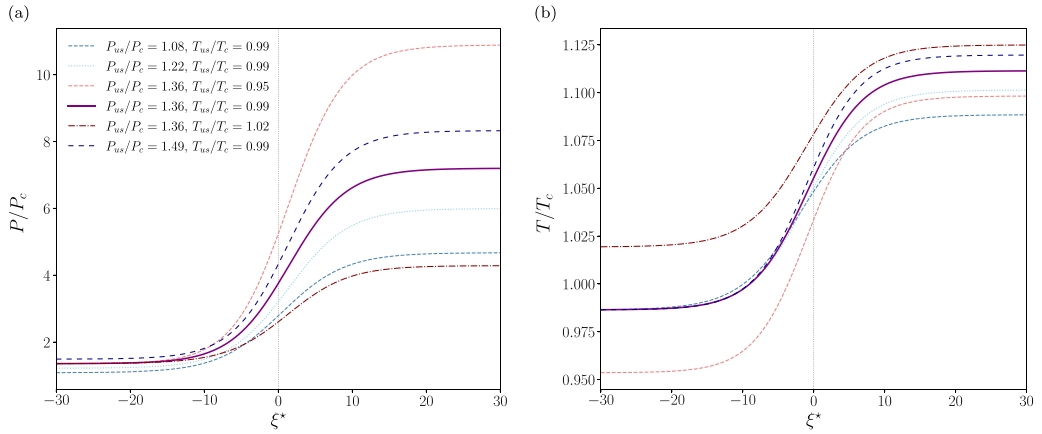


FIG. 6. Reduced pressure and temperature profiles for different upstream conditions at $\mathrm{Ma_{us}} = 1.5$.

all upstream conditions. In contrast with pressure and temperature, the density jump is only weakly affected by changes in the upstream thermodynamic state. Under the conditions studied in this work, this indicates that the flow does not experience the strong thermodynamic response typically associated with pseudophase transition, which can be assessed more directly by examining the temperature relative to the pseudoboiling temperature. In this regard, Fig. 7(b) shows the evolution of T/T_{pb} across the shock. In all cases, the profiles remain below unity, indicating that the local temperature does not reach the pseudoboiling condition. The thermodynamic path therefore remains within a single supercritical regime. Although the curves display nonmonotonic features, these are not indicative of a transition but rather reflect the coupled evolution of temperature and pressure through the shock. The origin of this behavior can be understood from the definition of the pseudoboiling temperature, which corresponds to the maximum of the isobaric heat capacity at a given pressure. As shown in Fig. 8(b), further increasing pressure reduces the magnitude of the maximum c_P and shifts it towards higher temperatures. As a result, the thermodynamic response associated with pseudoboiling becomes progressively weaker at high pressures. This behavior is reflected in the evolution of T_{pb} across the shock, shown in Fig. 8(a). For weaker shocks, T_{pb} varies smoothly, indicating that a well-defined pseudoboiling response still exists, even if it is not reached by the flow.

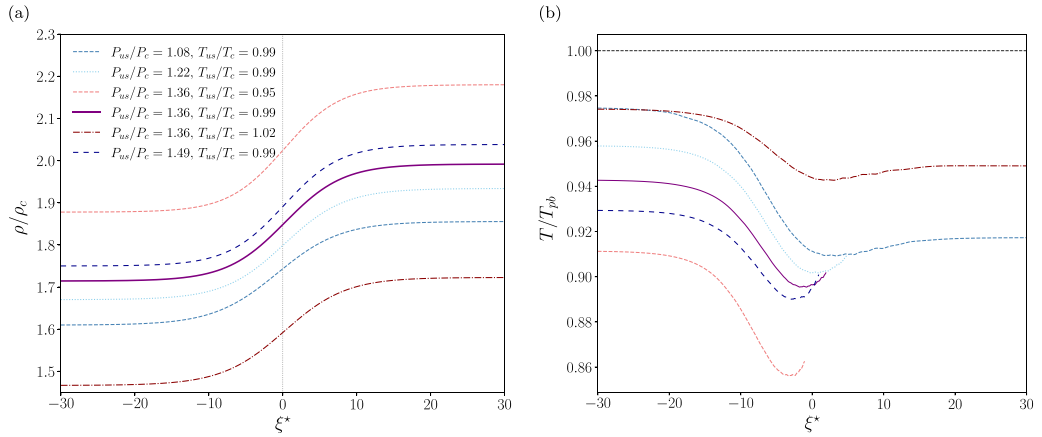


FIG. 7. Profiles for $\mathrm{Ma_{us}} = 1.5$ with different upstream conditions: (a) reduced density and (b) temperature normalized with the corresponding pseudoboiling temperature.

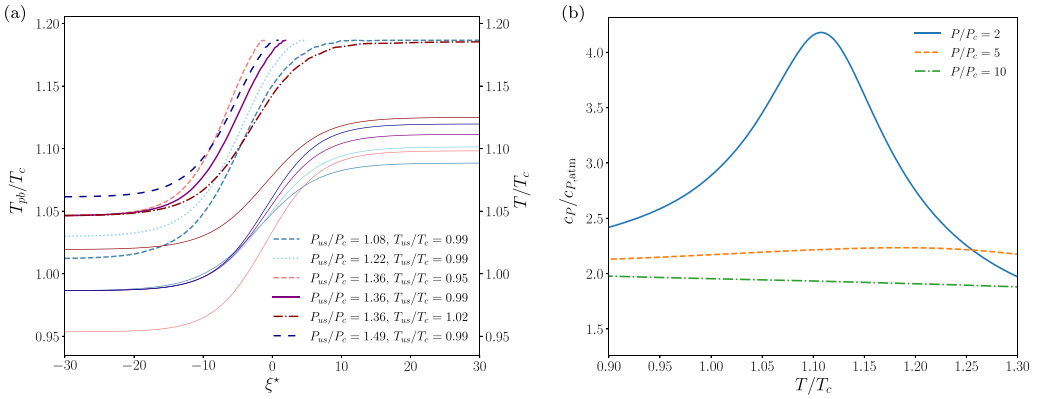


FIG. 8. Profiles for $\mathrm{Ma}_{\mathrm{us}} = 1.5$ with different upstream conditions: (a) pseudoboiling temperature normalized with the critical temperature and (b) isobaric heat capacity at $P/P_c = 2, 5, 10$ normalized by its reference value at atmospheric conditions $c_{P,\mathrm{atm}} = 850.85\ \mathrm{J/(kg\,K)}$.

For stronger shocks, the reduction and displacement of the c_P peak with increasing pressure weaken the thermodynamic response that defines the pseudoboiling transition. As a consequence, T_{pb} varies nonmonotonically along the shock and ceases to represent a clear transition between liquidlike and gaslike phase. Two distinct behaviors can therefore be identified. For weaker shocks, the flow remains below a still identifiable pseudoboiling line and the thermodynamic evolution is smooth. For stronger shocks at higher pressures, the distinction between liquidlike and gaslike states becomes less pronounced, and the pseudoboiling line is no longer sharply defined. In this regime, the flow may approach the nominal pseudoboiling condition, but this does not correspond to a well-defined thermodynamic transition due to the flattening of the c_P peak. In other words, the thermodynamic feature that defines pseudoboiling is no longer present along the supercritical path. Consequently, a pseudoboiling temperature T_{pb} cannot be identified, and the pseudoboiling line effectively ceases to exist in this regime. For this reason, T_{pb} is only reported in Figs. 7(b) and 8(a) under the range of conditions for which a c_P maximum remains identifiable. Overall, these results show that, under high-pressure supercritical conditions, the relevance of pseudoboiling depends strongly on the underlying thermodynamic response, which becomes progressively weaker as pressure increases. Ultimately, thermodynamic conditions determine the amplitude of the property variations, whereas the upstream velocity controls the shock structure. This distinction motivates the analysis of the shock thickness, which quantifies the spatial extent of the transition.

B. Shock thickness

The resolution of the shock-wave structure provides direct access to the spatial gradients of the thermodynamic and flow variables, from which the shock thickness can be evaluated *a posteriori*. A common definition is based on the maximum density gradient expressed as

$$\delta = \frac{\rho_{\mathrm{ds}} - \rho_{\mathrm{us}}}{\left.\frac{d\rho}{d\xi}\right|_{\mathrm{max}}}, \tag{9}$$

which relates the total density variation across the shock to the maximum local gradient, obtained from the shock solution. This definition therefore requires knowledge of the upstream and downstream states and is only applied after the shock solution has been obtained. The resulting thickness is expressed in units of the upstream mean-free path, which is used solely as the characteristic reference length for the nondimensional spatial coordinate.

Although viscosity and thermal conductivity are the mechanisms responsible for smoothing the discontinuity, they are not used as the direct definition of the thickness in this work. Instead, their

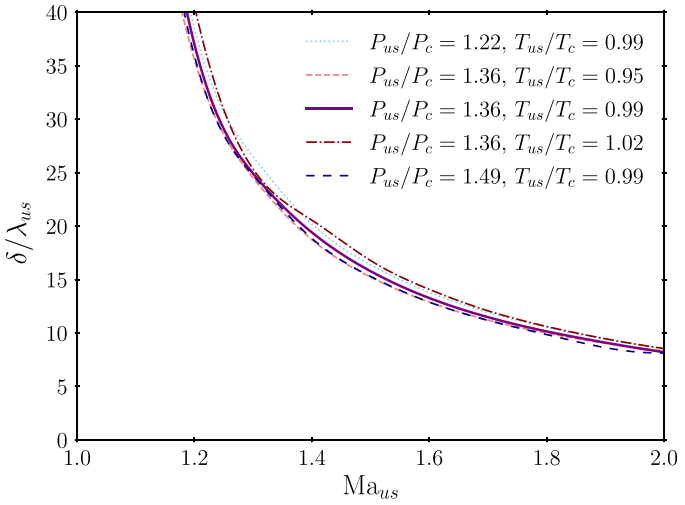


FIG. 9. Evolution of the shock-wave thickness with the upstream Mach number for different upstream conditions.

influence is incorporated through Eqs. (5) and (6), where all transport properties are evaluated as functions of the local thermodynamic state. This density-based definition is selected because it provides a direct measure of the spatial extent of the transition between the upstream and downstream states, allowing the effect of the real-fluid thermodynamic conditions to be analyzed consistently. In supercritical fluids, pressure and temperature define the thermodynamic state of the fluid and determine the corresponding transport properties, including viscosity and thermal conductivity, which are evaluated from the NIST database [52] throughout the shock structure.

Once the thickness is defined, it becomes possible to assess the relative influence of the upstream thermodynamic conditions and flow parameters. Figure 9 shows that the shock thickness is only weakly affected by upstream pressure and temperature, while it exhibits a strong dependence on the upstream Mach number. More specifically, the thickness decreases monotonically with increasing Mach number, following a hyperbolic trend consistent with previous studies [43]. This behavior can be understood from the balance between convection and diffusion within the shock layer. At low Mach numbers, close to the sonic limit, the shock is weak, meaning that the variations in flow properties across the discontinuity are small. As a result, the corresponding gradients are also weak, and the transition occurs over a relatively large spatial extent, leading to thick shock structures. In the limit as $\mathrm{Ma}_{\mathrm{us}} \to 1$, these gradients vanish and the shock thickness formally diverges, reflecting the disappearance of the discontinuity. Conversely, at sufficiently high Mach numbers, the shock thickness approaches values of $O(1)$ in mean-free-path units, suggesting that the structure becomes increasingly sharp. However, this reduction in spatial extent does not imply that the flow can be treated as ideal. While the spatial extent of the shock may become relatively small, the thermodynamic state at the boundaries continues to exhibit strong nonideal effects, particularly in dense-gas and supercritical-fluid regimes. Therefore, the validity of ideal-gas approximations must be assessed by considering both the internal structure and the upstream thermodynamic conditions. Only when high temperatures, sufficiently low densities, and large Mach numbers are simultaneously satisfied does the flow approach ideal behavior.

VI. CONCLUSION

This work has presented a real-fluid framework to analyze the structure of shock waves in dense-gas and supercritical-fluid regimes, removing the classical ideal-gas assumption. Starting

from the equations of fluid motion coupled with real-fluid thermodynamics, a set of conservation equations has been derived to resolve the internal structure of shocks. These equations were solved numerically using accurate thermophysical data for CO_2, allowing the independent effects of upstream pressure, temperature, and velocity to be systematically assessed. Both the jump conditions and the internal shock profiles were characterized across a wide range of thermodynamic states, providing a consistent description of compressive discontinuities in nonideal fluids.

The results demonstrate that real-fluid thermodynamics fundamentally alters the classical description of shock waves. The Euler-based jump relations dictate that the ideal-gas assumption fails to predict the admissible downstream states, with the upstream thermodynamic condition introducing an additional degree of freedom into the shock problem. It was confirmed that higher pressures amplify the nonideal response and increase the required compression, whereas increasing temperature drives the fluid towards ideal-gas behavior and reduces the deviation from Rankine-Hugoniot predictions. The internal shock analysis further revealed that thermodynamic and inertial effects influence different aspects of the shock structure. While the thermodynamic state governs the magnitude of the property variations across the shock, through its effect on enthalpy and compressibility, the upstream velocity determines the spatial organization of the transition by controlling the balance between convective transport and dissipative mechanisms. Consequently, the shock thickness remains primarily governed by the upstream Mach number, despite the strong modifications introduced by real-fluid thermodynamics in the jump conditions and thermodynamic profiles. This separation between shock intensity and shock structure represents a key distinction from the classical ideal-gas picture. Finally, the analysis of supercritical trajectories demonstrated that pseudoboiling effects must be interpreted according to the underlying thermodynamic response rather than solely by proximity to the pseudoboiling line. At sufficiently high pressures, the maximum in isobaric heat capacity weakens and the thermodynamic feature defining pseudoboiling disappears, making the concept of a pseudoboiling temperature progressively less meaningful for characterizing the shock evolution.

Future work can extend this framework to more complex configurations and fluid systems. In particular, the study of oblique shock waves in supercritical fluids would provide further insight into realistic aerodynamic applications. Extensions to multicomponent mixtures and reacting flows are also of interest, especially in the context of propulsion and energy systems. Future work could also extend this framework to fluids exhibiting nonconventional gas-dynamic behavior, including Bethe-Zel'dovich-Thompson fluids, where the thermodynamic convexity of the equation of state may lead to nonclassical wave phenomena. Furthermore, the analysis of supersonic expansions, as the counterpart of compressive shocks, would contribute to a more complete understanding of supercritical flow behavior in nozzles and high-speed devices. These directions would build upon the present framework to further characterize compressible flows under strongly nonideal conditions.

ACKNOWLEDGMENTS

This work was funded by the European Union (ERC, SCRAMBLE, Grant No. 101040379). The authors also acknowledge support from the SGR program (Grant No. 2021-SGR-01045) of Generalitat de Catalunya (Catalonia).

Views and opinions expressed are however those of the authors only and do not necessarily reflect those of the European Union or the European Research Council. Neither the European Union nor the granting authority can be held responsible for them.

DATA AVAILABILITY

The data that support the findings of this article are available upon reasonable request from the authors, although most of the presented results can be independently reproduced using the open-source solver provided in the accompanying repository [55].

APPENDIX A: DERIVATION OF THE CONSERVATION EQUATIONS FOR SHOCK-WAVE STRUCTURES

1. Temperature evolution expression

The conservation of total energy for the fluid system under adiabatic conditions, in the absence of body forces, is expressed as

$$\rho \frac{DE}{Dt} = -\nabla \cdot \boldsymbol{q} - \nabla \cdot (P\boldsymbol{u}) + \nabla \cdot (\boldsymbol{\tau} \cdot \boldsymbol{u}), \tag{A1}$$

where $E = e + \|\boldsymbol{u}\|^2/2$ and e are the specific total and internal energies, respectively. By substituting the relation $e = h - P/\rho$ and assuming a steady process, the following is obtained:

$$\rho \boldsymbol{u} \cdot \nabla h + \rho \boldsymbol{u} \cdot \nabla \left(\frac{\|\boldsymbol{u}\|^2}{2} \right) = -\nabla \cdot \boldsymbol{q} + \nabla \cdot (\boldsymbol{\tau} \cdot \boldsymbol{u}). \tag{A2}$$

Reducing the formulation to a 1D steady state yields

$$\rho u \frac{d}{dx} \left(h + \frac{u^2}{2} \right) = \frac{d}{dx} \left[\kappa \frac{dT}{dx} + \left(\mu_v + \frac{4}{3}\mu \right) \frac{du}{dx} u \right], \tag{A3}$$

where the viscous stress component is expressed in terms of the bulk viscosity μ_v and dynamic viscosity μ as $\tau_{xx} = (\mu_v + \frac{4}{3}\mu)\frac{du}{dx} = \mu_{\text{tot}}\frac{du}{dx}$, and the heat conduction flux follows Fourier's law, $q = -\kappa \frac{dT}{dx}$.

Given the continuity relation $\rho u = \rho_{\text{us}} u_{\text{us}}$, the first integration results in

$$\rho_{\text{us}} u_{\text{us}} \left(h + \frac{u^2}{2} \right) - u\mu_{\text{tot}} \frac{du}{dx} - \kappa \frac{dT}{dx} = C_1. \tag{A4}$$

By evaluating the energy flux at the upstream state ($x \to -\infty$), the integration constant is uniquely determined without requiring downstream information as

$$u = u_{\text{us}}, \quad T = T_{\text{us}}, \quad h = h_{\text{us}} \to \rho_{\text{us}} u_{\text{us}} \left(h_{\text{us}} + \frac{u_{\text{us}}^2}{2} \right) = C_1 \quad \text{as } x \to -\infty. \tag{A5}$$

Substituting C_1 back into Eq. (A4) gives

$$\rho_{\text{us}} u_{\text{us}} \left(h + \frac{u^2}{2} \right) - u\mu_{\text{tot}} \frac{du}{dx} - \kappa \frac{dT}{dx} = \left(h_{\text{us}} + \frac{u_{\text{us}}^2}{2} \right) \rho_{\text{us}} u_{\text{us}}. \tag{A6}$$

Similarly, integrating the 1D momentum-conservation equation (1b) in the form

$$\rho u \frac{du}{dx} + \frac{dP}{dx} - \frac{d}{dx} \mu_{\text{tot}} \frac{du}{dx} = 0 \tag{A7}$$

leads to

$$\mu_{\text{tot}} \frac{du}{dx} = \rho_{\text{us}} u_{\text{us}} (u - u_{\text{us}}) + (P - P_{\text{us}}). \tag{A8}$$

By inserting Eq. (A8) into Eq. (A6), the following expression is obtained:

$$(h - h_{\text{us}}) - \frac{1}{2}(u - u_{\text{us}})^2 - \frac{u}{\rho_{\text{us}} u_{\text{us}}} (P - P_{\text{us}}) - \frac{1}{\rho_{\text{us}} u_{\text{us}}} \kappa \frac{dT}{dx} = 0. \tag{A9}$$

Under the assumption that bulk viscosity is negligible in the upstream region, the total upstream viscosity is defined as $\mu_{\text{tot,us}} = \frac{4}{3}\mu_{\text{us}}$. The conservation equations are nondimensionalized using the properties of the upstream flow, with the dimensionless state variables and transport parameters defined as

$$h^\star = \frac{h}{u_{\text{us}}^2}, \quad u^\star = \frac{u}{u_{\text{us}}}, \quad \xi^\star = \frac{x}{\lambda_{\text{us}}}, \quad T^\star = \frac{T}{T_{\text{us}}}, \quad P^\star = \frac{P}{\rho_{\text{us}} u_{\text{us}}^2}, \quad \kappa^\star = \frac{\kappa}{\kappa_{\text{us}}}. \tag{A10}$$

By applying this nondimensionalization scheme to the energy equation, the dimensionless temperature evolution expression is obtained as

$$\frac{dT^\star}{d\xi^\star} = \frac{\mathrm{Re}_{\lambda,\mathrm{us}}\mathrm{Br}_{\mathrm{us}}}{\kappa^\star}\left((h^\star - h^\star_{\mathrm{us}}) - \frac{(u^\star-1)^2}{2} - u^\star(P^\star - P^\star_{\mathrm{us}})\right). \tag{A11}$$

2. Velocity evolution expression

The development starts by rearranging Eq. (A6) as

$$(h - h_{\mathrm{us}}) = \frac{1}{\rho_{\mathrm{us}}u_{\mathrm{us}}}u\mu_{\mathrm{tot}}\frac{du}{dx} + \frac{\kappa}{\rho_{\mathrm{us}}u_{\mathrm{us}}}\frac{dT}{dx} - \frac{1}{2}\left(u^2 - u^2_{\mathrm{us}}\right), \tag{A12}$$

and substituting this into Eq. (A9) yields

$$\frac{u\mu_{\mathrm{tot}}}{\rho_{\mathrm{us}}u_{\mathrm{us}}}\frac{du}{dx} - \frac{1}{2}\left(u^2 - u^2_{\mathrm{us}}\right) - \frac{1}{2}(u - u_{\mathrm{us}})^2 - \frac{u}{\rho_{\mathrm{us}}u_{\mathrm{us}}}(P - P_{\mathrm{us}}) = 0. \tag{A13}$$

The resulting nondimensional velocity evolution expression corresponds to

$$\frac{du^\star}{d\xi^\star} = \frac{\mathrm{Re}_{\lambda,\mathrm{us}}}{\mu^\star_{\mathrm{tot}}}[(1 - u^\star) + (P^\star - P^\star_{\mathrm{us}})]. \tag{A14}$$

3. Pressure evolution expression

The derivation begins with the 1D continuity equation for a steady flow, i.e., $d(\rho u)/dx = 0$, which can be expanded as

$$\rho\frac{du}{dx} + u\frac{d\rho}{dx} = 0. \tag{A15}$$

Rearranging this expression allows the spatial density evolution to be directly related to the variation of velocity as

$$\frac{d\rho}{dx} = -\frac{\rho}{u}\frac{du}{dx}. \tag{A16}$$

By applying the chain rule, the total differential of the density with respect to the spatial coordinate is also expressed in terms of pressure and temperature changes as

$$\frac{d\rho}{dx} = \left.\frac{\partial\rho}{\partial P}\right|_T\frac{dP}{dx} + \left.\frac{\partial\rho}{\partial T}\right|_P\frac{dT}{dx}. \tag{A17}$$

Equating these two expressions for $d\rho/dx$ yields the combined relation

$$-\frac{\rho}{u}\frac{du}{dx} = \left.\frac{\partial\rho}{\partial P}\right|_T\frac{dP}{dx} + \left.\frac{\partial\rho}{\partial T}\right|_P\frac{dT}{dx}. \tag{A18}$$

Solving for the pressure derivative dP/dx, the following expression is obtained:

$$\frac{dP}{dx} = -\frac{\frac{\rho}{u}\left(\frac{du}{dx}\right) + \left.\frac{\partial\rho}{\partial T}\right|_P\left(\frac{dT}{dx}\right)}{\left.\frac{\partial\rho}{\partial P}\right|_T}. \tag{A19}$$

In order to transform this equation to its nondimensional form, the dimensionless variables $P^\star = P/(\rho_{\mathrm{us}}u^2_{\mathrm{us}})$, $\rho^\star = \rho/\rho_{\mathrm{us}}$, $T^\star = T/T_{\mathrm{us}}$, and $\xi^\star = x/\lambda_{\mathrm{us}}$ are defined. Substituting these quantities into Eq. (A19) while incorporating the nondimensional isothermal compressibility $\beta^\star_T = \frac{1}{\rho^\star}\frac{\partial\rho^\star}{\partial P^\star}|_{T^\star}$ and thermal expansion coefficient $\alpha^\star_T = -\frac{1}{\rho^\star}\frac{\partial\rho^\star}{\partial T^\star}|_{P^\star}$ leads to the final nondimensional pressure evolution

expression

$$\frac{dP^\star}{d\xi^\star} = \frac{\frac{d\rho^\star}{d\xi^\star} - \frac{dT^\star}{d\xi^\star}\frac{\partial\rho^\star}{\partial T^\star}\big|_{P^\star}}{\frac{\partial\rho^\star}{\partial P^\star}\big|_{T^\star}} = \frac{1}{\rho^\star\beta_T^\star}\frac{d\rho^\star}{d\xi^\star} + \frac{\alpha_T^\star}{\beta_T^\star}\frac{dT^\star}{d\xi^\star}. \tag{A20}$$

APPENDIX B: RECOVERY OF THE IDEAL-GAS EXPRESSION

The derivation for the recovery of the ideal-gas expression begins with Eq. (A13) in the form

$$\frac{u\mu_{\text{tot}}}{\rho_{\text{us}}u_{\text{us}}}\frac{du}{dx} - \frac{1}{2}\left(u^2 - u_{\text{us}}^2\right) - \frac{1}{2}(u-u_{\text{us}})^2 - \frac{u}{\rho_{\text{us}}u_{\text{us}}}(P - P_{\text{us}}) = 0. \tag{B1}$$

As previously proven, the stagnation enthalpy remains constant such that $h + \frac{u^2}{2} = h_{\text{us}} + \frac{u_{\text{us}}^2}{2}$. Substituting the ideal-gas relation $h = c_P T$ into the previous equation, the temperature is expressed as

$$c_P T = \frac{\gamma}{\gamma - 1}R' T_{\text{us}} + \frac{u_{\text{us}}^2}{2} - \frac{u^2}{2}, \tag{B2}$$

where $\gamma = c_P/c_V$ is the ideal-gas heat capacity ratio and R' is the specific gas constant of the fluid under consideration. Neglecting the bulk viscosity μ_v for an ideal gas yields an effective total viscosity defined by $\mu_{\text{tot}} = \frac{4}{3}\mu$. By substituting Eq. (B2) into Eq. (B1), the following combined form is obtained:

$$\frac{4}{3}\frac{\mu}{\rho_{\text{us}}u_{\text{us}}}u\frac{du}{dx} - \frac{\gamma+1}{2\gamma}u^2 - \frac{\gamma-1}{2\gamma}u_{\text{us}}^2 + u_{\text{us}}u - R'T_{\text{us}} + \frac{u}{u_{\text{us}}}R'T_{\text{us}} = 0. \tag{B3}$$

To nondimensionalize the expression, the following dimensionless variables and relations are defined:

$$u^\star = \frac{u}{u_{\text{us}}}, \quad \xi^\star = \frac{x}{\lambda_{\text{us}}}. \tag{B4}$$

Furthermore, for ideal gases, the dynamic viscosity is a temperature-dependent variable $\mu = \mu(T)$, typically modeled through the power law

$$\mu = \mu_{\text{us}}\left(\frac{T}{T_{\text{us}}}\right)^n, \tag{B5}$$

where n is a positive constant that depends on the specific gas. In addition, the kinetic theory of gases [58] provides relations such as

$$\mu_{\text{us}} = \theta\rho_{\text{us}}\lambda_{\text{us}}\bar{c}_{\text{us}} = \theta\rho_{\text{us}}\lambda_{\text{us}}\sqrt{\frac{8R'T_{\text{us}}}{\pi}}, \tag{B6}$$

where $\theta = 0.35$ is a constant and $\bar{c} = \sqrt{\frac{8R'T}{\pi}}$ is the mean molecular velocity. Applying these definitions, Eq. (B3) transforms into

$$\frac{4}{3}\left[u^\star\left(\frac{T}{T_{\text{us}}}\right)^n\frac{\theta}{u_{\text{us}}}\sqrt{\frac{8R'T_{\text{us}}}{\pi}}\right]\frac{du^\star}{d\xi^\star} - \frac{\gamma+1}{2\gamma}u^{\star 2} - \frac{\gamma-1}{2\gamma} + u^\star + \frac{R'T_{\text{us}}}{u_{\text{us}}^2}(u^\star - 1) = 0. \tag{B7}$$

Finally, introducing the upstream Mach number $\text{Ma}_{\text{us}} = u_{\text{us}}/\sqrt{\gamma R'T_{\text{us}}}$ and the constants χ and α [43],

$$\chi = \frac{3}{8\theta}(\gamma+1)\sqrt{\frac{\pi}{8\gamma}}, \quad \alpha = \frac{\gamma-1}{\gamma+1} + \frac{2}{\gamma+1}\frac{1}{\text{Ma}_{\text{us}}^2}, \tag{B8}$$

the conservation equation is reduced to its final dimensionless form

$$T^{\star n} u^\star \frac{du^\star}{d\xi^\star} - \chi \, \mathrm{Ma}_{\mathrm{us}} (u^\star - 1)(u^\star - \alpha) = 0. \tag{B9}$$

This result recovers the foundational expressions established in previous works [22,43]. It should be noted that while the present framework is applicable to general gases, the specific expression derived by Patel and Singh [43] includes a factor $(u^\star - \bar{b})$ to account for nonideal excluded-volume effects; the expression (B9) is recovered in the limit where the nonidealness parameter $\bar{b}$ vanishes.

[1] J. Urzay, Supersonic combustion in air-breathing propulsion systems for hypersonic flight, Annu. Rev. Fluid Mech. **50**, 593 (2018).

[2] L. Fadigati, M. D. Gagliardi, E. Sozio, F. Rossi, N. Souhair, and F. Ponti, Aerospike aerodynamic characterization at varying ambient pressures, Aerospace **13**, 12 (2025).

[3] V. Raman, S. Prakash, and M. Gamba, Nonidealities in rotating detonation engines, Annu. Rev. Fluid Mech. **55**, 639 (2023).

[4] A. L. Kritcher, A. B. Zylstra, C. R. Weber, O. A. Hurricane, D. A. Callahan, D. S. Clark, L. Divol, D. E. Hinkel, K. Humbird, O. Jones, J. D. Lindl, S. Maclaren, D. J. Strozzi, C. V. Young, A. Allen, B. Bachmann, K. L. Baker, T. Braun, G. Brunton, D. T. Casey, *et al.*, Design of the first fusion experiment to achieve target energy gain $G > 1$, Phys. Rev. E **109**, 025204 (2024).

[5] J. H. S. Lee, *The Detonation Phenomenon* (Cambridge University Press, Cambridge, 2008).

[6] E. Wang, N. Peng, and M. Zhang, System design and application of supercritical and transcritical CO_2 power cycles: A review, Front. Energy Res. **9**, 723875 (2021).

[7] D. T. Banuti, Crossing the Widom-line – Supercritical pseudo-boiling, J. Supercrit. Fluids **98**, 12 (2015).

[8] L. Jofre and J. Urzay, Transcritical diffuse-interface hydrodynamics of propellants in high-pressure combustors of chemical propulsion systems, Prog. Energy Combust. Sci. **82**, 100877 (2021).

[9] B. E. Poling, J. M. Prausnitz, and J. P. O'Connell, *Properties of Gases and Liquids*, 5th ed. (McGraw-Hill, New York, 2001).

[10] O. A. Ladyzhenskaya, Mathematical analysis of Navier-Stokes equations for incompressible liquids, Annu. Rev. Fluid Mech. **7**, 249 (1975).

[11] J. D. Anderson, Jr., *Hypersonic and High-Temperature Gas Dynamics*, 2nd ed. (AIAA, Reston, 2006).

[12] W. J. M. Rankine, On the thermodynamic theory of waves of finite longitudinal disturbance, Philos. Trans. R. Soc. London 277 (1870).

[13] P.-H. Hugoniot, Mémoire sur la propagation du mouvement dans les corps et spécialement dans les gaz parfaits, J. Ec. Polytech. (Paris) **57**, 3 (1887).

[14] R. Menikoff and B. J. Plohr, The Riemann problem for fluid flow of real materials, Rev. Mod. Phys. **61**, 75 (1989).

[15] M. Ruggeri, I. Roy, M. J. Mueterthies, T. Gruenwald, and C. Scalo, Neural-network-based Riemann solver for real fluids and high explosives; application to computational fluid dynamics, Phys. Fluids **34**, 116121 (2022).

[16] R. Abgrall and V. Perrier, Asymptotic expansion of a multiscale numerical scheme for compressible multiphase flow, Multiscale Model. Simul. **5**, 84 (2006).

[17] J. W. Strutt, Aerial plane waves of finite amplitude, Proc. R. Soc. London Ser. A **84**, 247 (1910).

[18] G. I. Taylor, The conditions necessary for discontinuous motion in gases, Proc. R. Soc. A **84**, 371 (1910).

[19] R. Becker, Stoßwelle und detonation, Z. Phys. **8**, 321 (1922).

[20] L. H. Thomas, Note on Becker's theory of the shock front, J. Chem. Phys. **12**, 449 (1944).

[21] L. Meyerhoff, An extension of the theory of the one-dimensional shock-wave structure, J. Aeronaut. Sci. **17**, 775 (1950).

[22] M. Morduchow and P. A. Libby, On a complete solution of the one-dimensional flow equations of a viscous, heat-conducting, compressible gas, J. Aeronaut. Sci. **16**, 674 (1949).

[23] R. von Mises, On the thickness of a steady shock wave, J. Aeronaut. Sci. **17**, 551 (1950).
[24] C. Civrais, C. White, and R. Steijl, Extension of the normal shock wave relations for calorically imperfect gases, Shock Waves **33**, 533 (2023).
[25] R. Anand and H. Yadav, The effects of viscosity on the structure of shock waves in a non-ideal gas, Acta Phys. Pol. A **129**, 28 (2016).
[26] D. Khapra and A. Patel, Shock-wave structure in non-polar diatomic and polyatomic dense gases under rotation and vibration, Phys. Fluids **34**, 066115 (2022).
[27] D. Khapra and A. Patel, Shock wave structure in carbon dioxide using one and multi-temperature model, Indian J. Phys. **99**, 3365 (2025).
[28] M. S. Cramer and R. Sen, Exact solutions for sonic shocks in van der Waals gases, Phys. Fluids **30**, 377 (1987).
[29] P. A. Thompson, G. C. Carofano, and Y.-G. Kim, Shock waves and phase changes in a large-heat-capacity fluid emerging from a tube, J. Fluid Mech. **166**, 57 (1986).
[30] Q. Zhu, Y. Wu, W. Zhou, Q. Yang, and X. Xu, A comprehensive study on the roles of viscosity and heat conduction in shock waves, J. Fluid Mech. **984**, A74 (2024).
[31] M. Fathi, D. Roekaerts, and S. Hickel, Numerical simulation of transcritical multiphase combustion using real-fluid thermochemical and transport properties, Combust. Flame **275**, 114055 (2025).
[32] S. Chapman and T. G. Cowling, *The Mathematical Theory of Non-uniform Gases*, 3rd ed. (Cambridge University Press, Cambridge, 1970).
[33] C. Cercignani, *Theory and Application of the Boltzmann Equation* (Scottish Academic Press, Edinburgh, 1975).
[34] H. Struchtrup, Failures of the Burnett and super-Burnett equations in steady state processes, Continuum Mech. Thermodyn. **17**, 43 (2005).
[35] M. Torrilhon and H. Struchtrup, Regularized 13-moment equations: Shock structure calculations and comparison to Burnett models, J. Fluid Mech. **513**, 171 (2004).
[36] B. L. Hicks, S. M. Yen, and B. J. Reilly, The internal structure of shock waves, J. Fluid Mech. **53**, 85 (1972).
[37] E. Reyhanian, B. Dorschner, and I. Karlin, Kinetic simulations of compressible non-ideal fluids: From supercritical flows to phase-change and exotic behavior, Computation **9**, 13 (2021).
[38] A. Guardone, P. Colonna, M. Pini, and A. Spinelli, Nonideal compressible fluid dynamics of dense vapors and supercritical fluids, Annu. Rev. Fluid Mech. **56**, 241 (2024).
[39] N. R. Nannan, C. Sirianni, T. Mathijssen, A. Guardone, and P. Colonna, The admissibility domain of rarefaction shock waves in the near-critical vapour–liquid equilibrium region of pure typical fluids, J. Fluid Mech. **795**, 241 (2016).
[40] N. Alferez and E. Touber, One-dimensional refraction properties of compression shocks in non-ideal gases, J. Fluid Mech. **814**, 185 (2017).
[41] E. Touber and N. Alferez, Shock-induced energy conversion of entropy in non-ideal fluids, J. Fluid Mech. **864**, 807 (2019).
[42] C. C. Conti, A. Fusetti, A. Spinelli, and A. Guardone, Shock loss measurements in non-ideal supersonic flows of organic vapors, Exp. Fluids **63**, 117 (2022).
[43] A. Patel and M. Singh, Exact solution of shock wave structure in a non-ideal gas under constant and variable coefficient of viscosity and heat conductivity, Shock Waves **29**, 427 (2019).
[44] C. C. Wu and P. H. Roberts, Shock-wave propagation in a sonoluminescing gas bubble, Phys. Rev. Lett. **70**, 3424 (1993).
[45] P. H. Roberts and C. C. Wu, Structure and stability of a spherical implosion, Phys. Lett. A **213**, 59 (1996).
[46] J. Vishwakarma and G. Nath, A self-similar solution of a shock propagation in a mixture of a non-ideal gas and small solid particles, Meccanica **44**, 239 (2009).
[47] D. Li, J. Komperda, A. Peyvan, Z. Ghiasi, and F. Mashayek, Assessment of turbulence models using DNS data of compressible plane free shear layer flow, J. Fluid Mech. **931**, A10 (2022).
[48] A. Firoozabadi, *Thermodynamics and Applications in Hydrocarbon Energy Production*, 1st ed. (McGraw-Hill, New York, 2016).

[49] G. Soave, Equilibrium constants from a modified Redlich-Kwong equation of state, Chem. Eng. Sci. **27**, 1197 (1972).
[50] D.-Y. Peng and D. B. Robinson, A new two-constant equation of state, Ind. Eng. Chem. Fund. **15**, 59 (1976).
[51] I. H. Bell, J. Wronski, S. Quoilin, and V. Lemort, Pure and pseudo-pure fluid thermophysical property evaluation and the open-source thermophysical property library CoolProp, Ind. Eng. Chem. Res. **53**, 2498 (2014).
[52] P. J. Linstrom and W. G. Mallard, Thermophysical properties of fluid systems, NIST Chemistry WebBook (SRD 69) (NIST, Gaithersburg, 2023), https://webbook.nist.gov/chemistry/fluid.
[53] E. Kustova, M. Mekhonoshina, A. Bechina, S. Lagutin, and Y. Voroshilova, Continuum models for bulk viscosity and relaxation in polyatomic gases, Fluids **8**, 48 (2023).
[54] F. Jaeger, O. K. Matar, and E. A. Müller, Bulk viscosity of molecular fluids, J. Chem. Phys. **148**, 174504 (2018).
[55] K. Foley-Valledor, Shock-wave structure solver, GitHub, 2026, https://github.com/foleyvak/Shock_Wave_Structure_Solver.
[56] M. S. Cramer and G. M. Tarkenton, Transonic flows of Bethe–Zel'dovich–Thompson fluids, J. Fluid Mech. **240**, 197 (1992).
[57] W. C. Reynolds and P. Colonna, *Thermodynamics: Fundamentals and Engineering Applications*, 1st ed. (Cambridge University Press, Cambridge, 2019).
[58] L. B. Loeb, *Kinetic Theory of Gases*, 1st ed. (McGraw-Hill, New York, 1927), p. 187.